Artificial Intelligence in Geosciences 6 (2025) 100111

Contents lists available at ScienceDirect

Artificial Intelligence in Geosciences

journal homepage: www.keaipublishing.com/en/journals/artificial-intelligence-in-geosciences

Enhancing understanding of 3D rectangular tunnel heading stability in *c*-φ soils with surcharge loading: A comprehensive FELA analysis using three stability factors and machine learning

Suraparb Keawsawasvong [a], Jim Shiau [b], Nhat Tan Duong [c,d], Thanachon Promwichai [a], Rungkhun Banyong [a], Van Qui Lai [c,d,*]

[a] Research Unit in Sciences and Innovative Technologies for Civil Engineering Infrastructures, Department of Civil Engineering, Thammasat School of Engineering, Thammasat University, Pathumthani, 12120, Thailand

[b] School of Engineering, University of Southern Queensland, Toowoomba, 4350, QLD, Australia

[c] Faculty of Civil Engineering, Ho Chi Minh City University of Technology (HCMUT), 268 Ly Thuong Kiet Street, District 10, Ho Chi Minh City, Viet Nam

[d] Vietnam National University Ho Chi Minh City (VNU-HCM), Linh Trung Ward, Thu Duc District, Ho Chi Minh City, Viet Nam

ARTICLE INFO

Keywords:
3D tunnel
Stability factors
Terzaghi
Superposition
FELA
ANN
XGBoost

ABSTRACT

This study examines the stability of three-dimensional rectangular tunnel headings in drained *c*-ϕ soils, incorporating surcharge effects using 3D Finite Element Limit Analysis (FELA). It focuses on the upper and lower bound solutions for three stability factors: cohesion, surcharge, and soil unit weight (Nc, Ns, and Nγ). Based on Terzaghi's principle of superposition, the analysis evaluates tunnel stability under varying parameters, such as cover-depth ratio (H/D), width-depth ratio (B/D), and friction angle (ϕ). The results align closely with previous studies, and practical design charts are provided for calculating minimum support pressures. Additionally, machine learning models (ANN and XGBoost) are used to develop accurate correlations between input parameters and stability results. A relative importance index analysis is conducted to assess the impact of these parameters. This research enhances understanding of tunnel stability and offers practical insights for tunnel design.

1. Introduction

Rectangular tunnels are commonly used in urban areas for transportation, utilities, pedestrian passageways, mining, and various other purposes. They offer efficient use of space, and therefore are particularly well-suited for utility applications, such as for electrical cables, water pipes, or sewage systems. Although rectangular tunnels may not always be the first choice in terms of tunnel geometry, they have experienced increased popularity due to their distinct benefits.

Ensuring the stability of tunnels is one of the central challenges in the field of geotechnical engineering. For this purpose, various researchers have employed the Finite Element Limit Analysis (FELA) method to evaluate safety factors or collapse loads in diverse geotechnical problems (Drucker et al., 1952; Chen and Liu, 2012; Sloan, 2013; Sangjinda et al., 2023). Earlier research focused on tunnel stability has presented upper bound (UB) and lower bound (LB) solutions for various tunnel shape and soil condition including circular tunnel in undrained soil (Wilson et al., 2011; Shiau and Keawsawasvong, 2022; Keawsawasvong and Ukritchon, 2022), drained soil (Yamamoto et al., 2011a; Xiao et al., 2019a) and rock masses (Zhang et al., 2019). Furthermore, there were several studies on square and rectangular shape tunnel stability for drained and undrained (Sloan and Assadi, 1991, Yamamoto et al., 2011b; Abbo et al., 2013; Wilson et al., 2015; Xiao et al., 2019b; Bhattacharya and Dutta, 2023). Recent studies have significantly enhanced the understanding of tunnel stability, including research on shield tunnels such as tail grout performance (Liang et al., 2024), partial blowout instability (Liu et al., 2024), and working face stability in inclined tunnels (Wu et al., 2024). These studies have contributed to a deeper understanding of grout behavior, face stability, and the challenges posed by various soil conditions. However, a comprehensive examination of

Peer review under the responsibility of KeAi Communications Co., Ltd.

* Corresponding author. Faculty of Civil Engineering, Ho Chi Minh City University of Technology (HCMUT), 268 Ly Thuong Kiet Street, District 10, Ho Chi Minh City, Viet Nam.

E-mail addresses: ksurapar@engr.tu.ac.th (S. Keawsawasvong), jim.shiau@usq.edu.au (J. Shiau), dntan.sdh231@hcmut.edu.vn (N.T. Duong), thanachon.pr@outlook.co.th (T. Promwichai), rungkhun.ban@gmail.com (R. Banyong), lvqui@hcmut.edu.vn (V.Q. Lai).

https://doi.org/10.1016/j.aiig.2025.100111
Received 20 June 2024; Received in revised form 3 February 2025; Accepted 9 March 2025
Available online 14 March 2025

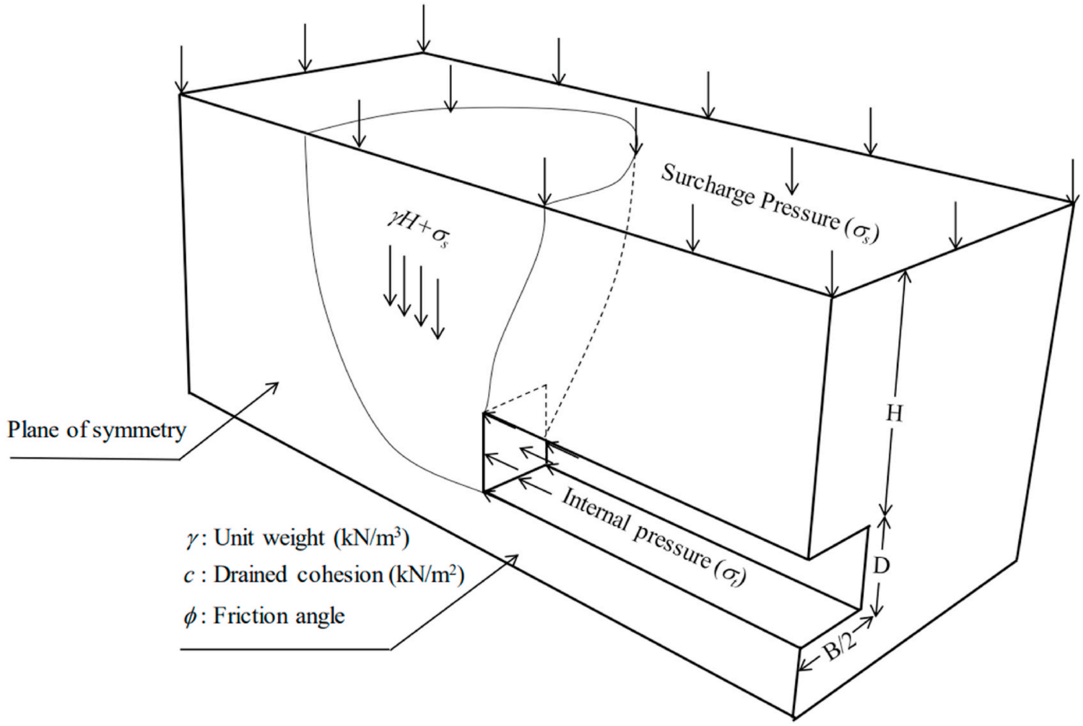

Fig. 1. Problem definition – rectangular tunnel heading.

the stability of rectangular tunnels in drained c-ϕ soils under surcharge pressure was not found in the literature. This highlights the need for thorough investigation and extensive research in this particular area.

As a pioneering work, Atkinson and Mair (1981) introduced a drained stability solution to compute the minimum support pressure (σ_t) required for collapse in shield tunnels in cohesionless soil. Consequently, Anagnostou and Kovári 1996 extended their proposal by introducing a stability equation which accommodates cohesive, frictional, and cohesive-frictional soils in their study, despite of the limited results produced. Vermeer et al., (2002) utilized the displacement finite element method to investigate shield tunnel face stability, employing a stepwise-reduced support pressure technique. They concluded that the stability factor F_γ remains unaffected by the tunnel depth when friction angles are greater than twenty degrees. On the other hand, Qarmout et al., (2019) introduced a novel two-block failure mechanism for upper bound analysis, enabling them to determine tunnel stability factors for shallow circular tunnels. They reported that the shape of the equivalent area of the tunnel face has minimal impact on the minimum support pressure, and that F_γ increases as the friction angle decreases.

In a recent study by Shiau and Al-Asadi (2020a), an in-depth investigation to tunnel stability have been conducted utilizing a three-factor approach. Their research specifically focused on analyzing the stability of drained tunnel headings in a two-dimensional (2D) space, utilizing the rigorous upper and lower bound finite element limit analysis. Expanding upon their previous work, Shiau and Al-Asadi 2020b-c further extended the three-factor approach to the problem of 3D circular tunnel heading stability and 3D twin circular tunnel headings. However, it is important to note that none of these studies have specifically investigated the 3D tunnel stability in relation to rectangular shape using the three-factor approach for studying drained c-ϕ soils with surcharge effects.

Various machine learning (ML) methods, such as Artificial Neural Network (ANN) and Extreme Gradient Boosting (XGBoost), have been incorporated into geotechnical engineering studies for solving complex problems (Shahin et al., 2001; Zhu et al., 2021; Lai et al. 2022, 2023, Nguyen et al. 2023a-b). On the one hand, ANN, which appeared in earlier research, is a basic model whose capacity is not only to produce explicit prediction functions but also to investigate the importance of each input parameter (Lai et al., 2022, Nguyen et al. 2023a-b, Azim, 2022). On the other hand, XGBoost is a technique published recently that can solve classification and regression problems with highly accurate results (Shekar et al., 2024). As a result, it is one of the most popular algorithms used in winning models in Kaggle competitions (Chen and Guestrin, 2016).

This paper aims to address this research gap by conducting a numerical investigation into the three-dimensional drained stability of rectangular tunnel headings. To achieve this objective, we employed Finite Element Limit Analysis (FELA) framework, incorporating both upper bound (UB) and lower bound (LB) methods. The primary focus is to determine the three stability factors, namely the cohesion factor N_c, surcharge factor N_s, and the unit weight factor N_γ, that can be used with the modified Terzaghi's equation to determine a critical boundary pressure at a collapse state. Moreover, the study provides practical design charts and equations that enable a quick estimation of minimum support pressure. By thoroughly exploring the three-dimensional drained stability of rectangular tunnels and accounting for surcharge pressure effects, the result of the present study will enhance our understanding on the stability characteristics and provide valuable insights for efficient and reliable tunnel design practices. One additional goal in the paper is to use Artificial Neural Network (ANN) and Extreme Gradient Boosting (XGBoost) to machine learning the dataset produced by the rigorous upper and lower bound results of the three factors. The optimal technique for this tunnel problem would be chosen based on their performance, proposing the prediction model for practical designs in future applications.

2. Problem description and FELA modelling

The problem to be investigated is shown in Fig. 1, where the geometric arrangement of a three-dimensional (3D) rectangular tunnel is presented in a symmetrical domain in 3D. The soil medium surrounding the tunnel is simulated as drained soil based on the Mohr-Coulomb yield criterion, and it is assumed to be both homogeneous and isotropic. The soil profile is influenced by three strength parameters: soil unit weight

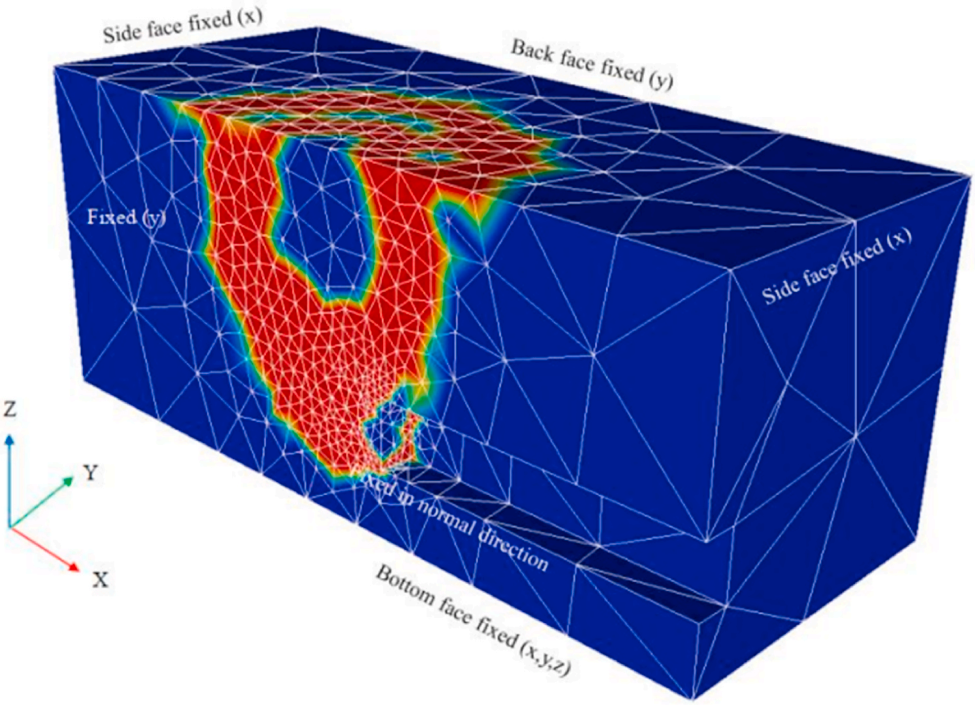

Fig. 2. A numerical model, adaptive mesh, and shear dissipation (N_c, $H/D = 4$, and $B/D = 1$).

(γ), drained cohesion (c), and friction angle (ϕ). It is acknowledgeable that, the Mohr-Coulomb yield criterion is a simplifying assumption for geotechnical analyses and is a common practice in tunnel stability assessments.

The tunnel's geometry is characterized by its width (B) and height (D). The cover-depth is H from the ground surface to the top of the rectangular tunnel. A uniform internal pressure (σ_t) is applied on the tunnel's face, while a vertical surcharge pressure (σ_s) is imposed downward on the ground surface.

For the proposed 3D tunnel face problem, soil stability can be expressed by Terzaghi's modified bearing capacity equation to calculate a minimum support pressure, as stated in equation (1).

$$\sigma_t = -cN_c + \sigma_s N_s + \gamma D N_\gamma \tag{1}$$

where N_c is the cohesion factor, N_s is the surcharge factor, and N_γ is the unit weight factor. In particular, the negative sign for the cohesion term indicates that cN_c is a resisting agency acting against the surcharge and the soil self-weight. Similar to Terzaghi's bearing capacity factors, these tunnel stability factors are functions of the soil internal friction angle (ϕ) as well as two geometric parameters, namely the cover-depth ratio (H/D) and the width-depth ratio (B/D).

The computational strategy adopted for calculating (N_c, N_s, and N_γ) is based on the principal of superposition as shown in equation (1). In the current analysis, the assumption of a weightless soil ($\gamma = 0$) was made for the purpose of simplifying the model. This theoretical simplification allowed for a focused investigation of the relationships between these parameters without the added complexity of soil weight. However, it is important to note that this assumption deviates significantly from actual conditions, where the unit weight of the soil is always positive. It is essential to note the specific assumptions in each type of analysis and the reduced equations as shown in Eq. (2).

- For N_c, the computation involves no surcharge load ($\sigma_s = 0$) and no soil unit weight ($\gamma = 0$).
- For N_s, it is hypothesized that a cohesionless soil ($c = 0$) and a weightless soil ($\gamma = 0$) exist.
- For N_γ, both cohesion and surcharge are assumed to be zero ($c = 0$ and $\sigma_s = 0$) in the computation.

$$\begin{pmatrix} N_c = -\sigma_t/c \\ N_s = \sigma_t/\sigma_s \\ N_\gamma = \sigma_t/\gamma D \end{pmatrix} = f\left(\frac{H}{D}, \frac{B}{D}, \phi\right) \tag{2}$$

Finite Element Limit Analysis is a powerful and rigorous numerical technique for assessing the stability and collapse behavior of soil structures subjected to various loading conditions. In this method, upper bound (UB) and lower bound (LB) estimates are used to bracket the true collapse load for practical uses (Sloan, 2013). The origins of Finite Element Limit Analysis can be traced back to the pioneering works of Sloan, 1988, 1989. Initially, the technique incorporated linear programming to develop the Finite Element Limit Analysis (FELA). More recent developments have introduced significantly faster and more efficient nonlinear programming formulations, as demonstrated by the work of Lyamin and Sloan, 2002a, 2002b, as well as the contributions of Krabbenhoft et al., (2007). The fundamental principles of bound theorems are based on the assumption of a rigid-perfectly plastic material with associated plasticity. In recent times, the application of FELA has been widely spread to solve diverse stability problems in geotechnical engineering, both in drained and undrained soil conditions (Shiau and Yu, 2000; Shiau and Al-Asadi, 2020c, 2020d, 2022; Shiau et al., 2022 Huynh et al., 2022; Lai et al., 2022).

This paper utilized OptumG3 in combination with rigorous finite element upper and lower bound techniques to compute stability solutions of the three stability factors for the tunnel heading problem. Fig. 2 presents a typical numerical model for the analysis. The soil mass is represented by using the Mohr-Coulomb constitutive model with associated flow rule. The numerical models are simulated using the following boundary conditions: the model's side face is fixed along the x-direction (normal direction), while the back and front faces are restricted in the y-direction (normal direction). The bottom boundary is fixed in all directions, i.e., no movement allowed in the x, y, and z-directions. In contrast, both the ground surface and the inner tunnel face are free surfaces, allowing unrestricted movement in any direction. It should be noted that the term "inner tunnel face" refers to the excavation

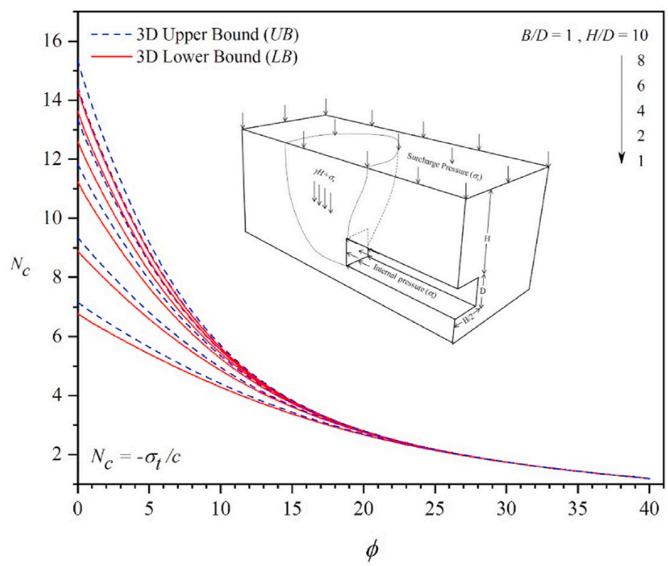

Fig. 3. N_c vs ϕ for various depth ratios ($H/D = 1$–10, UB and LB, and $B/D = 1$).

face of the tunnel, while the side face is fixed in normal direction. The assumption of free surfaces at both the ground surface and the excavation face was made to simplify the model and focus on the ultimate failure conditions, assuming no external restraint on the surrounding soil. It is imperative that the model domain be relatively large, encapsulating potential collapsible areas, so that the accuracy of numerical solutions can be sustained.

The present numerical analysis employs adaptive meshing technique. With the use of shear dissipation function to identify sensitive zones, the technique dynamically modified the mesh during the interactive analysis, with more refined meshes along the potential slip surface. This approach would greatly improve the upper and lower bound solutions. In this paper, the adaptive meshing function is iteratively applied five repetitions, gradually increasing the number of discretization elements from 5,000 to 10,000. It should be emphasized that the initial number of 5,000 elements and the number of optimization iterations of 5 were selected to balance mesh refinement and computational efficiency. Further iterations could theoretically improve mesh quality, it was observed that further iterations beyond the fifth had minimal impact on the results, while significantly increasing computational costs, particularly given the need to run multiple cases. This approach aligns with similar studies in this field, where 5 iterations have proven to be adequate for obtaining reliable results without excessive computational demand. More importantly, the resulting final adaptive mesh would exhibit a meshing pattern that resembles a failure mechanism. This can be viewed in Fig. 2 with non-zero shear power dissipation. This figure showcases the numerical model of the three-dimensional rectangular tunnel, with particular focus on the N_c parameter, while adopting specific parameter values of $H/D = 4$ and $B/D = 1$. As discussed by Shiau and Al-Asadi 2020a-b, the actual values of these non-zero shear power dissipation are not important, and therefore they are not typical shown in a technical report.

With this computational procedure, a bulk of parametric studies are performed, aiming to produce rigorous solutions of the three stability factors (N_c, N_s, and N_γ). The chosen ranges of parameters are for $H/D =$ 1–10, $B/D = 0.5$–5, and the drained friction angle ($\phi = 0$–$40°$). Specifically, the study examined the influence of variations in cohesion, friction angle, surcharge, and unit weight on the three stability factors. By understanding the interrelationships among N_c, N_s, and N_γ, it provides critical design parameters that can be utilized to estimate the critical minimum support pressure (σ_t) required to prevent tunnel collapse particularly when these parameters exhibit significant variability due to changes in local soil properties or external loading conditions.

3. Results and discussion

A comprehensive set of 1080 Finite Element Limit Analysis (FELA) analyses is simulated in this study. The cohesion, surcharge, and unit weight factors (N_c, N_s, and N_γ) are systematically varied, using different cover depth ratios ($H/D = 1$–10), width-depth ratios ($B/D = 0.5$–5), and the soil's internal friction angle ($\phi = 0$–$40°$). The upper and lower bound solutions are employed to provide a range of potential collapse load outcomes. The upper bound provides an overestimate, assuming an idealized, most efficient failure mechanism, which ensures that the collapse load is not underestimated. In contrast, the lower bound provides a more conservative estimate, based on a less efficient failure mechanism, offering a safeguard against overestimating the collapse load. This dual approach enhances the reliability of the results by establishing a bracket within which the true collapse load is likely to lie and allows for validation against previous studies. The obtained results provide a thorough understanding of the tunnel's behavior under the effects of these varying parameters. In the subsequent sections, detailed numerical results of (N_c, N_s, and N_γ) will be discussed respectively.

3.1. The cohesion factor N_c

3D numerical analyses for the cohesion factors (N_c) requires certain specific assumptions, such as surcharge pressure ($\sigma_s = 0$) and weightless soil ($\gamma = 0$). Under these conditions, the tunnel heading stability equation (1) reduces to $\sigma_t = -cN_c$, and therefore $N_c = -\sigma_t/c$.

Fig. 3 presents upper and lower bound results of N_c for the various values of $\phi = 0$–$40°$ and $H/D = 1$–10 with a fixed B/D value of 1. The data used to prepare the figure is shown in Table 1. In general, the greater the H/D, the larger the N_c, and the value of N_c decreases with increasing ϕ. Noting the different rates of decrease for the H/D curves, they all merge into a single line after $\phi > 20°$. In other words, the effect of H/D on N_c is literally the same after $\phi > 20°$, even though when ϕ reaches 40°, the N_c value is practically negligibly small. This suggests that the soil strength reaches its ultimate state, rendering the negligible cohesion effects. For such a 3D problem, the development of strong soil arching for large values of ϕ cannot be underestimated.

Using the same data as in Table 1, presented in Fig. 4 is for upper and lower bound results of N_c for $\phi = 0$–$40°$, $H/D = 5$, and $B/D = 0.5$–5. These results show that N_c decreases at various gradients as ϕ increases. Indeed, wider tunnels would create a more susceptible collapse area, and thus smaller values of N_c are expected. The smaller the B/D, the larger the N_c, and thus the larger the rate of decrease. Nevertheless, they all merge into a single curve at approximate $\phi = 19°$, owing to the development of soil arches for large soil internal friction angles ϕ.

3.2. The surcharge factor N_s

The computational strategy for the surcharge factors (N_s) requires specific assumptions in the input, namely $c = 0$ and $\gamma = 0$. With these conditions, the tunnel heading stability equation (1) is simplified to $\sigma_t = \sigma_s N_s$, and thus $N_s = \sigma_t/\sigma_s$. Fig. 5 shows the results of upper and lower bound solution of N_s for the various values of $\phi = 0$–$40°$ and $H/D = 1$–10 with a fixed B/D value of 1.

Numerical results in Fig. 5 show a maximum value of $N_s = 1$ at $\phi =$ 0 for all values of H/D. The value of N_s exhibits a dramatic linear decline (nearly by half) for the range of ϕ value between 0 and 5. However, once ϕ exceeds 5, the rate of reduction starts to decrease, and the curves become nonlinear. Subsequently, when ϕ surpasses 15°, N_s reaches its minimum value and eventually drops to 0 at $\phi = 20°$ for deep tunnels ($H/D > 4$). For shallow tunnels ($H/D = 1$ and 2), they are more susceptible to the influence of surcharge. Therefore, it is conservative to state that N_s approaches zero at $\phi = 30°$. Practically, that means the effect of H/D on N_s is none for $\phi > 30°$ due to the soil arching

Table 1
3D N_c data.

3D N_c (LB) for ($B/D = 1$)										
ϕ	$H/D = 1$	2	3	4	5	6	7	8	9	10
0	6.772	8.891	10.227	11.235	11.997	12.606	13.092	13.616	13.877	14.361
1	6.448	8.363	9.491	10.326	11.005	11.470	11.893	12.264	12.644	12.851
5	5.377	6.505	7.088	7.476	7.764	7.956	8.135	8.263	8.380	8.494
10	4.248	4.764	4.986	5.096	5.195	5.243	5.294	5.326	5.357	5.376
15	3.345	3.548	3.616	3.645	3.666	3.679	3.689	3.693	3.700	3.703
20	2.643	2.714	2.724	2.728	2.732	2.739	2.740	2.741	2.742	2.745
25	2.122	2.133	2.137	2.138	2.140	2.142	2.142	2.143	2.144	2.144
30	1.725	1.728	1.725	1.729	1.730	1.729	1.728	1.730	1.731	1.730
35	1.425	1.424	1.426	1.426	1.425	1.426	1.427	1.427	1.426	1.427
40	1.187	1.190	1.189	1.189	1.190	1.190	1.189	1.191	1.191	1.191
3D N_c (UB) for ($B/D = 1$)										
ϕ	$H/D = 1$	2	3	4	5	6	7	8	9	10
0	7.149	9.362	10.803	11.831	12.669	13.356	13.915	14.456	14.941	15.348
1	6.799	8.765	9.991	10.850	11.515	12.094	12.561	12.947	13.349	13.669
5	5.597	6.715	7.331	7.713	7.987	8.207	8.388	8.529	8.657	8.764
10	4.357	4.855	5.055	5.180	5.263	5.320	5.357	5.389	5.413	5.436
15	3.394	3.581	3.639	3.664	3.681	3.693	3.699	3.706	3.708	3.712
20	2.670	2.723	2.735	2.738	2.738	2.739	2.744	2.744	2.744	2.745
25	2.127	2.138	2.142	2.142	2.142	2.143	2.143	2.144	2.144	2.144
30	1.726	1.731	1.731	1.730	1.730	1.730	1.731	1.731	1.729	1.729
35	1.426	1.426	1.423	1.426	1.427	1.426	1.427	1.426	1.428	1.426
40	1.190	1.190	1.190	1.188	1.191	1.190	1.191	1.191	1.191	1.191

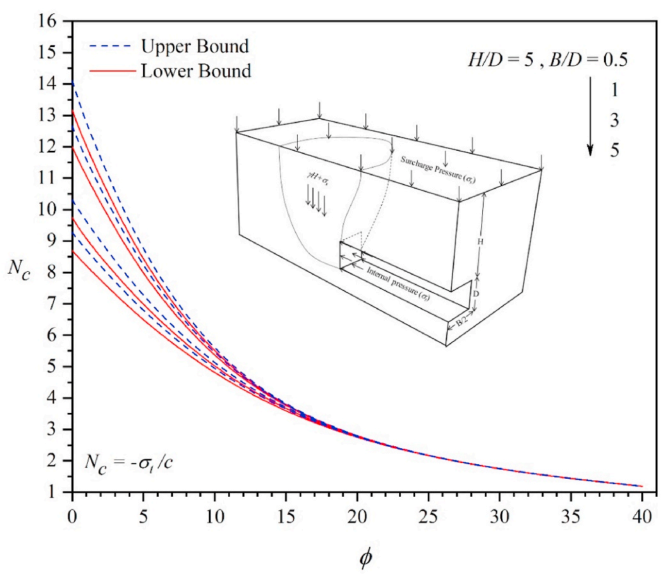

Fig. 4. N_c vs ϕ for various width ratios (B/D = 0.5–50, UB and LB, and H/D = 5).

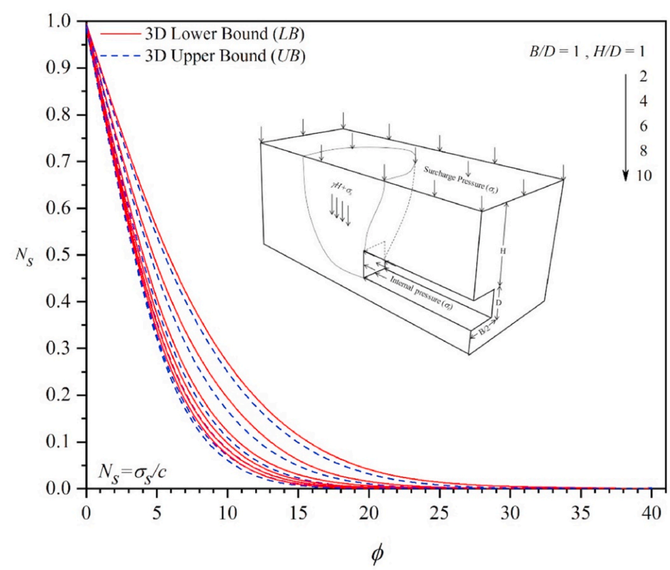

Fig. 5. N_s vs ϕ for various depth ratios (H/D = 1–10, UB and LB, and B/D = 1).

development at large internal friction angles of soils, and therefore the larger the H/D the smaller the N_s. The data used to prepare Fig. 5 is shown in Table 2.

Shown in Fig. 6 are for upper and lower bound results of N_s for (B/D = 0.5–5, ϕ = 0–40°, and H/D = 5). Similarly, N_s shows a decreasing trend as ϕ increases. As B/D increases (wider tunnel), N_s also increases. Similar observation made earlier in Fig. 5 is repeated here in this scenario. Specifically, as $\phi > 20°$ a variation of B/D ratio has no effect on the value of N_s. It can therefore be concluded that the surcharge factor N_s has a more pronounced impact on wider tunnels, as compared to narrower ones.

3.3. The unit weight factor N_γ

To reach a solution for the unit weight factors (N_γ), equation (1) is reduced to $\sigma_t = \gamma D N_\gamma$, and thus $N_\gamma = \sigma_t / \gamma D$. For this purpose, ($c = 0$ and $\sigma_s = 0$) are the two important inputs for the solutions. Fig. 7 presents the numerical results of the upper and lower bound solutions of N_γ for the various values of ϕ = 0–40° and H/D = 1–10 with a fixed B/D value of 1. The data used to prepare the figure is shown in Table 3. These results show the non-linear decreasing relationship between N_γ and ϕ. An increase in ϕ leads to a nonlinear reduction in N_γ. The variation of H/D plays a significant role on N_γ, in particular, for the lower values of $\phi <$ 20°, where the larger the H/D, the greater the N_γ. Interestingly, all H/D curves merge into one as ϕ is approximately greater than 20°. As commonly known, the larger the soil internal friction angle ϕ, the greater the soil arching, and therefore resulting in smaller values N_γ. Besides, N_γ is negligibly small owing to the development of strong soil arching with large values of ϕ in such a 3D tunnel heading problem.

Selected numerical results from Fig. 7 are used to showcase the effect B/D on N_γ in Fig. 8, where the relationship between N_γ and ϕ is shown

Table 2
3D N_s data.

3D N_s (*LB*) for ($B/D = 1$)										
ϕ	$H/D = 1$	2	3	4	5	6	7	8	9	10
0	0.995	0.991	0.990	0.989	0.988	0.987	0.987	0.986	0.986	0.986
5	0.526	0.428	0.372	0.339	0.319	0.296	0.280	0.269	0.261	0.250
10	0.248	0.172	0.118	0.094	0.079	0.069	0.061	0.056	0.050	0.046
15	0.101	0.046	0.028	0.021	0.014	0.011	0.008	0.007	0.005	0.003
20	0.034	0.011	0.006	0.004	0.002	0.002	0.001	0.000	0.000	0.000
25	0.011	0.002	0.002	0.001	0.001	0.001	0.001	0.001	0.000	0.000
30	0.004	0.000	0.000	0.000	0.000	0.000	0.000	0.000	0.000	0.000
35	0.002	0.001	0.000	0.000	0.000	0.000	0.000	0.000	0.000	0.000
40	0.000	0.000	0.000	0.000	0.000	0.000	0.000	0.000	0.000	0.000
3D N_s (*UB*) for ($B/D = 1$)										
ϕ	$H/D = 1$	2	3	4	5	6	7	8	9	10
0	0.993	0.991	0.990	0.988	0.988	0.987	0.986	0.986	0.985	0.985
5	0.505	0.405	0.351	0.318	0.293	0.273	0.258	0.234	0.230	0.224
10	0.227	0.139	0.102	0.081	0.068	0.057	0.050	0.046	0.035	0.034
15	0.085	0.037	0.022	0.014	0.010	0.007	0.004	0.004	0.003	0.002
20	0.025	0.006	0.002	0.000	0.000	0.000	0.000	0.000	0.000	0.000
25	0.005	0.000	0.001	0.001	0.001	0.002	0.002	0.000	0.000	0.000
30	0.001	0.001	0.000	0.000	0.000	0.000	0.000	0.000	0.000	0.000
35	0.001	0.000	0.001	0.000	0.000	0.000	0.000	0.000	0.000	0.000
40	0.000	0.001	0.001	0.000	0.000	0.000	0.000	0.000	0.000	0.000

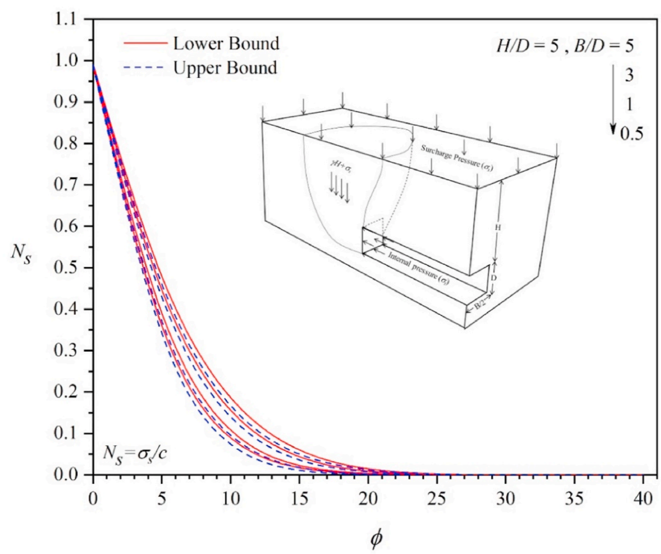

Fig. 6. N_s vs ϕ for various width ratios ($B/D = 0.5$–5, *UB* and *LB*, and $H/D = 5$).

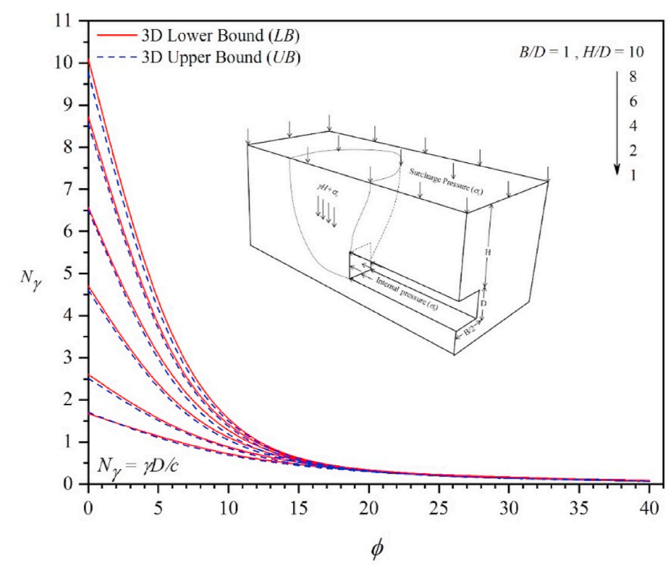

Fig. 7. N_γ vs ϕ for various depth ratios ($H/D = 1$–10, *UB* and *LB*, and $B/D = 1$).

for $H/D = 5$ and $B/D = 0.5$–5. The variation of N_γ begins approximately from ($H/D + 0.5$) at $\phi = 0°$, i.e., 5.5 in this case. Thereafter, a nonlinear decreasing relationship is observed, in particularly, when ϕ is less than 25°. A higher B/D ratio leads to a greater N_γ value. This can be attributed to the fact that widening the tunnel would result in larger unsupported length, thus increasing the likelihood of collapse, thus leading to greater support of σ_t. On the other hand, in the case of stronger soils ($\phi > 25°$), the N_γ values for all B/D scenarios are similarly small. It can therefore be concluded that the variation in B/D has insignificant effect on N_γ when dealing with soils that possess high internal frictional angles ϕ.

In this section, numerical results of the three factors are compared with those in Shiau and Al-Asadi 2020a-b. Shiau and Al-Asadi's investigation included stability solutions for two types of tunnels: 2D plain strain tunnels heading and 3D circular tunnel heading. The comparisons are for the three distinct factors, namely N_c, N_s, and N_γ. These factors play crucial roles in determining the stability of the tunnel, and the series of comparison are presented in Figs. 9–17, providing a comprehensive understanding of how the current results deviate or align with the findings from Shiau and Al-Asadi's studies.

4. Comparison with others

4.1. Comparison of N_c

In Fig. 9, the current N_c results are compared to those reported by Shiau and Al-Asadi 2020a-b. For shallow tunnel cases where $H/D = 1$, it is evident that the 2D plain strain N_c results give the lowest values. This is because the 2D plain strain analysis assumes infinite length, leading to conservative solutions when compared to the more realistic three-dimensional analysis. Interestingly, both the three-dimensional results for rectangular and circular tunnel shapes exhibit the same trend. When considering deeper tunnels (H/D = 5 and 10), similar patterns are observed, reaffirming the reliability and accuracy of the current N_c results, as shown in Figs. 10 and 11.

Table 3
3D N_γ data.

3D N_γ (*LB*) for ($B/D = 1$)										
ϕ	$H/D = 1$	2	3	4	5	6	7	8	9	10
0	1.675	2.601	3.586	4.709	5.574	6.576	7.554	8.727	9.665	10.102
5	1.121	1.478	1.824	2.139	2.432	2.712	2.961	3.212	3.457	3.692
10	0.689	0.835	0.929	1.001	1.062	1.109	1.161	1.196	1.240	1.272
15	0.454	0.489	0.505	0.515	0.521	0.527	0.532	0.540	0.535	0.539
20	0.306	0.312	0.313	0.313	0.313	0.313	0.314	0.315	0.319	0.320
25	0.216	0.216	0.215	0.215	0.215	0.213	0.214	0.218	0.219	0.216
30	0.156	0.157	0.156	0.155	0.159	0.156	0.157	0.168	0.151	0.156
35	0.117	0.117	0.116	0.115	0.118	0.116	0.116	0.117	0.116	0.117
40	0.087	0.086	0.088	0.087	0.087	0.087	0.086	0.087	0.088	0.088
3D N_γ (*UB*) for ($B/D = 1$)										
ϕ	$H/D = 1$	2	3	4	5	6	7	8	9	10
0	1.889	2.513	3.577	4.606	5.372	6.514	7.281	8.569	9.395	9.780
5	1.064	1.431	1.767	2.060	2.328	2.570	2.814	3.112	3.337	3.466
10	0.659	0.812	0.872	0.935	0.980	1.011	1.121	1.154	1.222	1.252
15	0.429	0.432	0.466	0.472	0.478	0.476	0.512	0.481	0.474	0.516
20	0.287	0.288	0.284	0.283	0.286	0.289	0.289	0.286	0.289	0.296
25	0.201	0.199	0.200	0.197	0.195	0.193	0.194	0.187	0.189	0.186
30	0.142	0.144	0.144	0.143	0.142	0.133	0.134	0.130	0.131	0.130
35	0.102	0.107	0.105	0.105	0.104	0.106	0.099	0.099	0.107	0.108
40	0.078	0.079	0.077	0.076	0.077	0.065	0.071	0.069	0.068	0.070

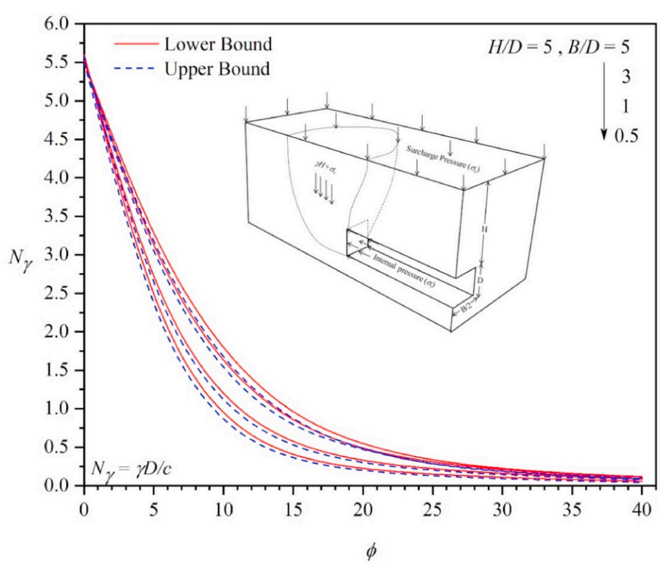

Fig. 8. N_γ vs ϕ for various width ratios ($B/D = 0.5$–5, *UB* and *LB*, and $H/D = 5$).

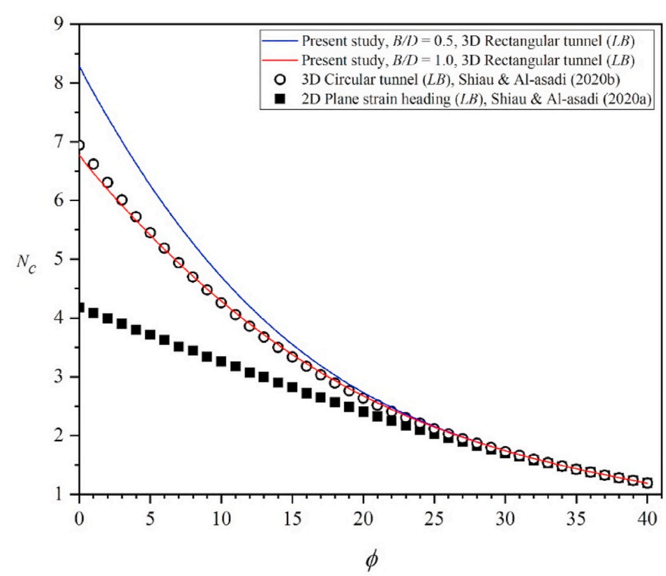

Fig. 9. Comparison of N_c ($H/D = 1$).

4.2. Comparison of N_s

Moreover, Figs. 12–14 show the comparison between the current N_s results and those presented by Shiau and Al-Asadi 2020a-b for $H/D = 1$, 5, and 10. Across all three comparisons, an identical trend is observed, with N_s having the most significant impact on the 2D plain strain tunnel. This is because the infinite length assumption in the 2D plain strain analysis is conservative, and it allows the surcharge pressure to be efficiently transmitted along the entire tunnel. However, it is noteworthy that for all H/D ratios, the same pattern emerges, ensuring the accuracy and reliability of the present solution. The consistency of the results across different H/D ratios indicates that the current analysis method effectively captures the surcharge factor's influence on the stability of the rectangular tunnel.

4.3. Comparison of N_γ

Lastly, the comparison between the current N_γ results and those presented by Shiau and Al-Asadi 2020a-b are demonstrated in Figs. 15–17 for $H/D = 1$, 5, and 10. The present study demonstrates a striking similarity between the N_γ results and those obtained from the 3D circular tunnel analysis, across all values of H/D. Notably, the N_γ factor continues to exert the most profound influence on the 2D plain strain tunnel as mentioned previously, owing to its conservative solutions.

Overall, a notable level of comparability and excellent agreement is evident between the three stability factors presented in this study and the findings from the preceding research conducted by Shiau and Al-Asadi 2020a-b. Among these factors, the 3D circular stability analysis exhibits the closest resemblance, underscoring the reliability of the computed FELA solutions in practice.

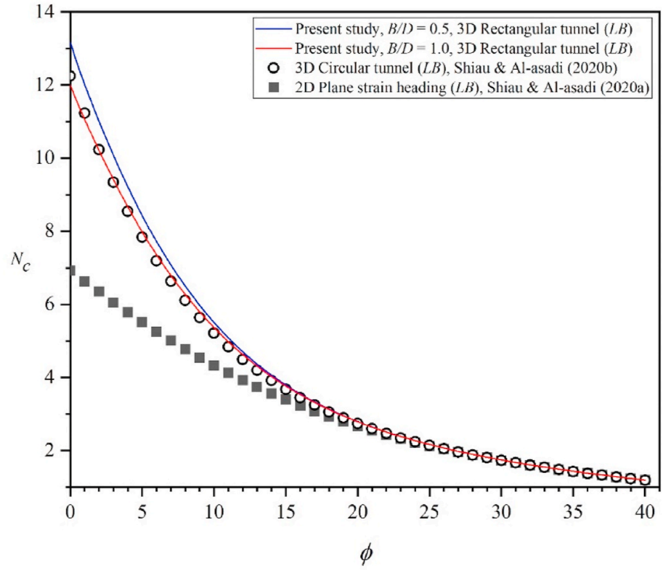

Fig. 10. Comparison of N_c ($H/D = 5$).

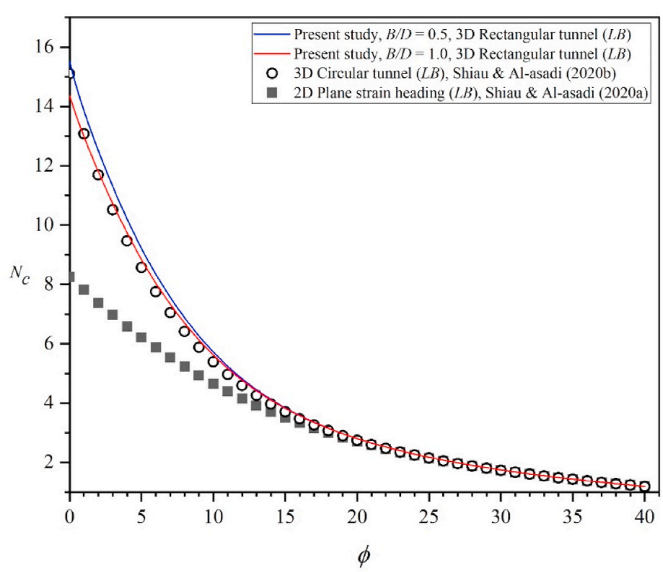

Fig. 11. Comparison of N_c ($H/D = 10$).

5. Machine learning methods

5.1. Artificial Neural Networks (ANN)

The ANN models in this study have three neural layers: an input layer, a hidden layer, and an output layer. The details are conceptually illustrated in Fig. 18, where (ϕ, H/D, and B/D) are input parameters in the input layer. Combining these with the weight and bias matrices in the hidden layer, a predictive model can be developed. As shown in the output layer, it has six outputs ($N_{c,LB}$, $N_{c,UB}$, $N_{s,LB}$, $N_{s,UB}$, $N_{\gamma,LB}$, and $N_{\gamma,UB}$).

Note that the speed and performance of the training process are affected by the parameters related to the algorithm and the ANN architecture. Since the last decade, various algorithms for training ANN models have been invented, including Levenberg Marquardt, Stochastic Gradient Descent, Bayesian Regularization, and Adaptive Moment Estimation (Adam). Notably, Adam is the method published by Kingma and Ba (2014), which has been successfully applied in a wide range of studies (Pandey et al., 2022; Zhang et al., 2019; Rozante et al., 2023).

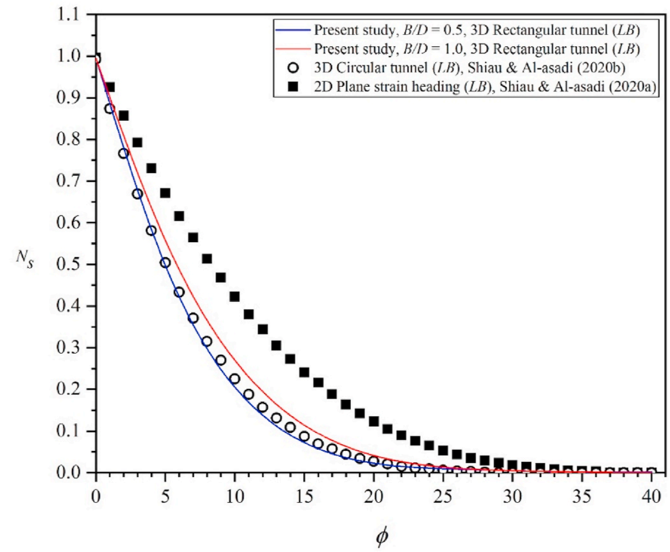

Fig. 12. Comparison of N_s ($H/D = 1$).

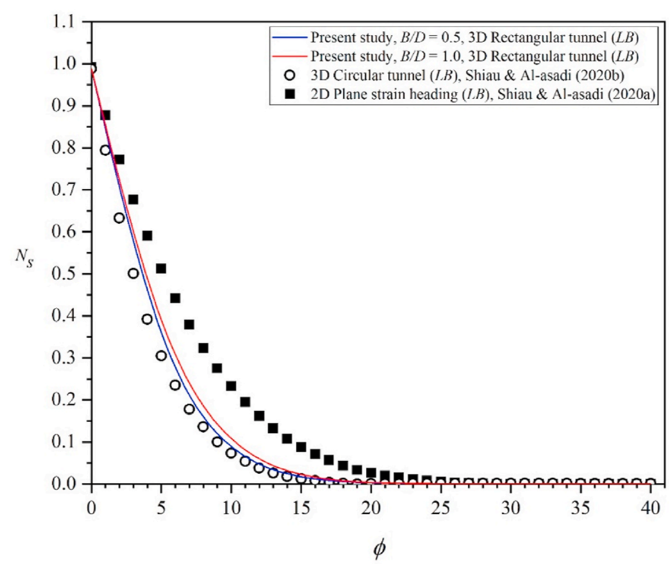

Fig. 13. Comparison of N_s ($H/D = 5$).

Therefore, we have decided to employ this algorithm in this study. The properties and procedures are described in Table 4 and Fig. 18, respectively.

The structure of each ANN model is presented by the number of hidden neurons, archiving its optimal value through a process of varying and testing the prediction's accuracy of each model (Lai et al., 2022; Nguyen et al., 2023a). In order to introduce non-linearity and enable the network to approximate complex functions, activation functions are used in the hidden layers of neural networks. These functions may include hyperbolic tangent, linear transfer function, sigmoid function, and rectified linear unit function. Note that the choice of activation function can affect the performance of the network, and different functions may be more suitable for different types of problems and architectures. In this paper, the first two functions (i.e., hyperbolic tangent and linear transfer function) are selected for the hidden nodes and the six output nodes, respectively, as recommended by previous geotechnical studies (Lai et al., 2022; Nguyen et al., 2023a) with significant accuracy in their ANN models' predictions. The hyperbolic tangent, also called *tansig*, is described in Eq. (3), while the final prediction is

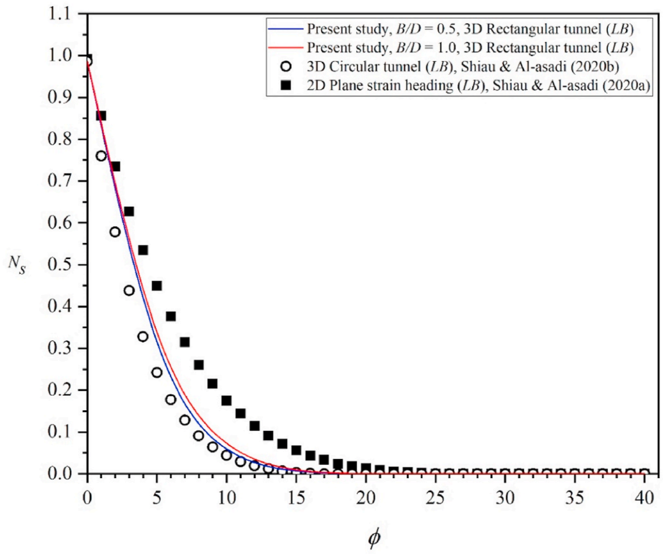

Fig. 14. Comparison of N_s ($H/D = 10$).

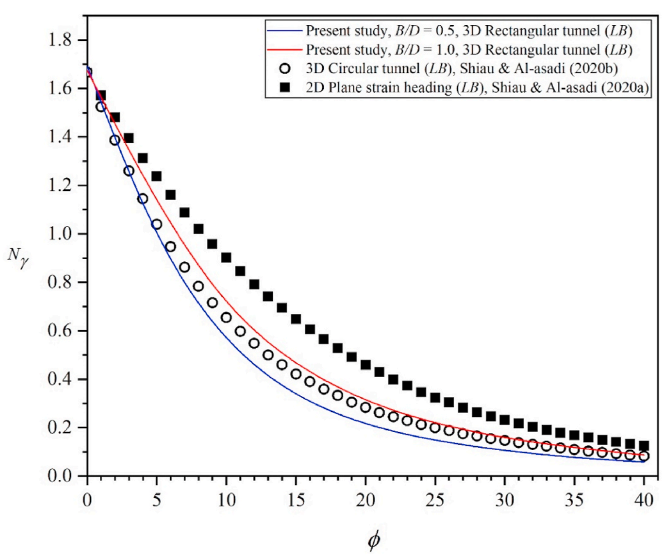

Fig. 15. Comparison of N_γ ($H/D = 1$).

indicated in Eq. (4).

$$tansig(x) = tanh(x) = \frac{2}{1 + e^{-2x}} - 1 \tag{3}$$

$$\text{Prediction} = \sum_{i=1}^{N_h} W^{2,i} tansig\left(\sum_{j=1}^{J} W^{1,i}x^j + b^{1,i}\right) + b^{2,i} \tag{4}$$

5.2. Extreme Gradient Boosting (XGBoost)

XGBoost, proposed by Chen and Guestrin (2016), is a method based on the gradient boosting technique. In the geotechnical field, it has been implemented to solve both classification and regression problems, producing the prediction with significant accuracy (Zhu et al., 2021; Lai et al., 2023).

An XGBoost model contains a sequence of weak models, which are binary regression trees in general regression problems. Each weak learner has two critical properties: the tree's maximum depth and the number of leaf nodes, also called terminal nodes. At each non-terminal node, the binary regression tree separates its data into two groups by

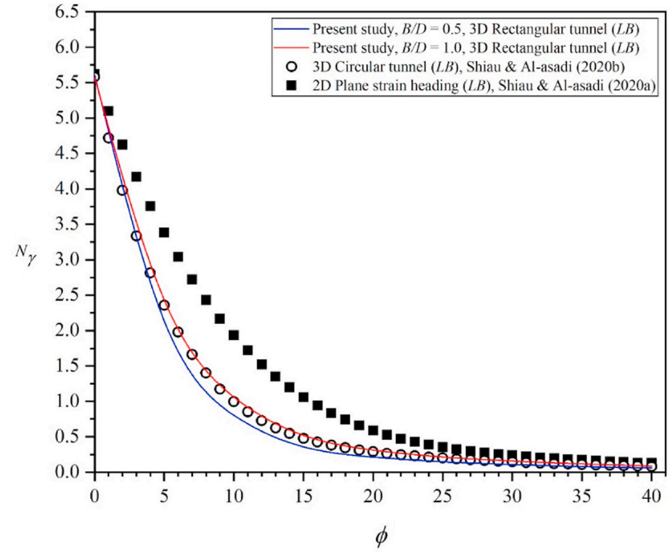

Fig. 16. Comparison of N_γ ($H/D = 5$).

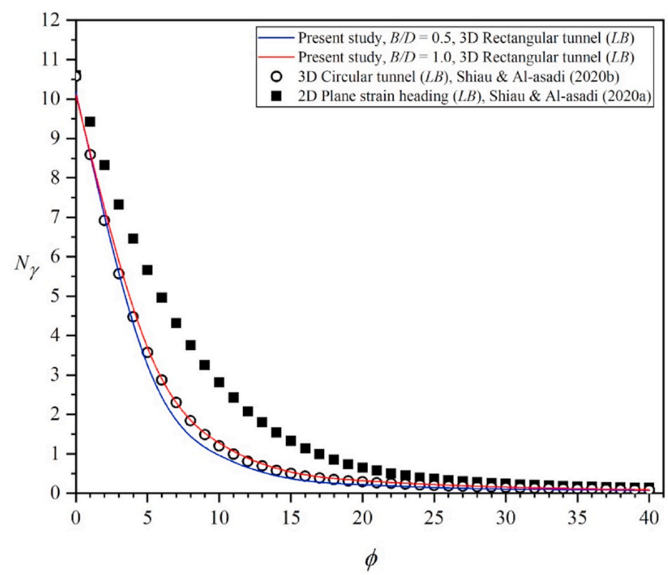

Fig. 17. Comparison of N_γ ($H/D = 10$).

choosing a value that reduces the largest error. Given the preset values, a shallow tree will be grown until it reaches the possible largest size. Nevertheless, this growing process has a high risk of overfitting, especially with a large-size tree. Therefore, instead of just minimizing the model's error, the model is provided by a penalizing term, as shown in Eq. (5).

$$R_a(T) = R(T) + a\left|\widetilde{T}\right| \tag{5}$$

Here, *R(T)* is the error of the regression tree; $|\widetilde{T}|$ is the number of leaf nodes, and α is the trade-off factor between the model's accuracy and its size. The right-size tree, with minimum error, can be archived by testing or cross-validation.

This machine learning method aims to create a set of regression trees in the form of Eq. (6). In that, K represents the number of weak learners; $f_k(x, \Theta_k)$ denotes the output of the kth tree with its structure Θ_k, and $\widehat{y}_k$ denotes the prediction by the first k regression trees. Besides, a learning rate ν is introduced to reduce every tree's prediction, and $0 < \nu < 1$.

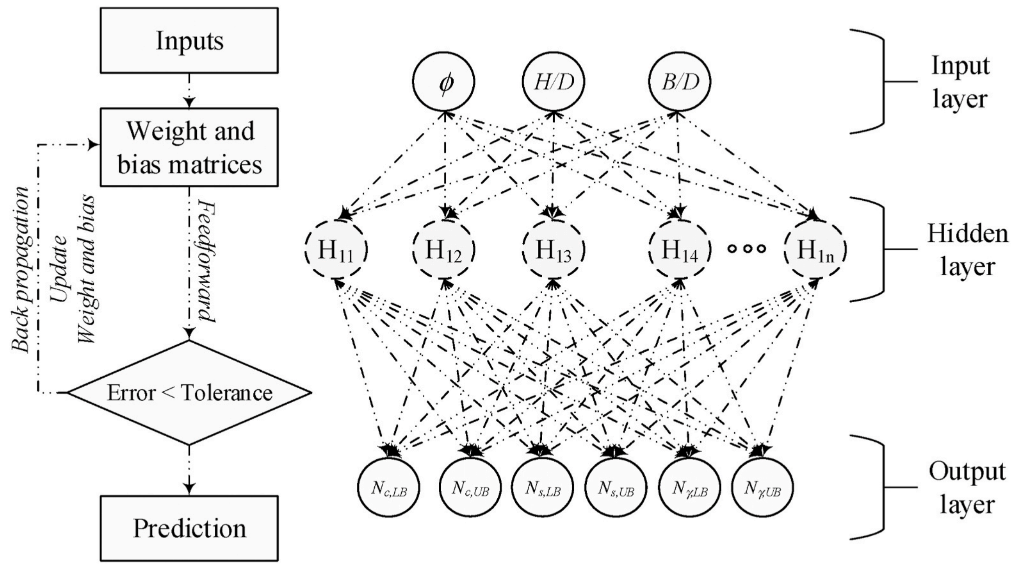

Fig. 18. The ANN model: components and training process.

Table 4
Preset values of four ADAM parameters.

Hyper-parameter	Explanation	Value
β_1	Exponential decay rate of first moment vector	0.9
β_2	Exponential decay rate of second moment vector	0.999
α	Learning rate	0.0001
ε	Numerical stability	10^{-8}

$$\hat{y}_K = \nu \sum_{k=1}^{K} f_k(x, \Theta_k) \tag{6}$$

$$L = \sum_{n=1}^{N} l(y_i, \hat{y}_i) + \sum_{k=1}^{K} \Omega(f_k) \tag{7}$$

$$\Omega(f_k) = \gamma T_k + \frac{1}{2}\lambda \sum_{i=1}^{T_k} w_k^i \tag{8}$$

Regarding the process described in Fig. 19, XGBoost adds a new weak learner at every step, minimizing the first term in Eq. (6) until the preset number of weak learners is met. However, this can create an overfitting model, given a large number of shallow trees. Therefore, the second term $\Omega(f_k)$ indicated in Eq. (6), also called the regularization function, is added to the target function to be minimized. The function $\Omega(f_k)$ plays a role as a trade-off component between the accuracy and complexity of the model, decreasing the chance of overfitting. In Eqs. (7) and (8), w_k^i is the weight of the ith terminal node, and T_k is the number of terminal nodes of the k^{th} tree. Besides, γ is the required minimum loss reduction to divide the current node, and λ is regarded as the regularization factor.

5.3. Data collection and performance measurements

A set of 540 results from the FELA method is used to train ANN and XGBoost models. Specifically, the whole data set is divided into the training set and testing set with the proportion of 70 % (378 data points) and 30 % (162 data points), respectively. It is reasonable that the data in these groups has relatively similar statistical properties (Zhu et al., 2021; Nguyen et al., 2023b). Table 5 presents these aspects with the upper and lower bounds, mean, and standard deviation (SD) of data in the two sets.

R-squared (R^2), Root Mean Square Error (*RMSE*), and Mean Absolute Error (*MAE*) indicated in Eqs. (9) and (10) are used to evaluate the performance of each machine learning model. More specifically, the nearer the R^2 is to 1.0, the better the ML model performs. By contrast, the further *RMSE* and *MAE* are from 0.0, the worse the prediction becomes.

Table 5
The statistical values of data in training and testing sets.

Variable	Training set (70 % data)				Testing set (30 % data)			
	Max	Min	Mean	SD	Max	Min	Mean	SD
ϕ	40	0	21.0	13.1	40	0	17.6	12.2
B/D	10	1	5.4	2.8	10	1	5.6	3.0
H/D	5	0.5	2.6	1.6	5	0.5	2.6	1.6

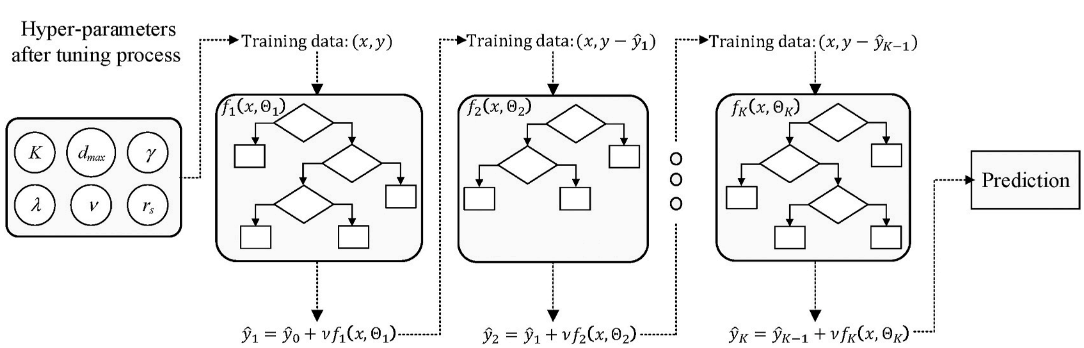

Fig. 19. The tuning and training procedure of XGBoost models.

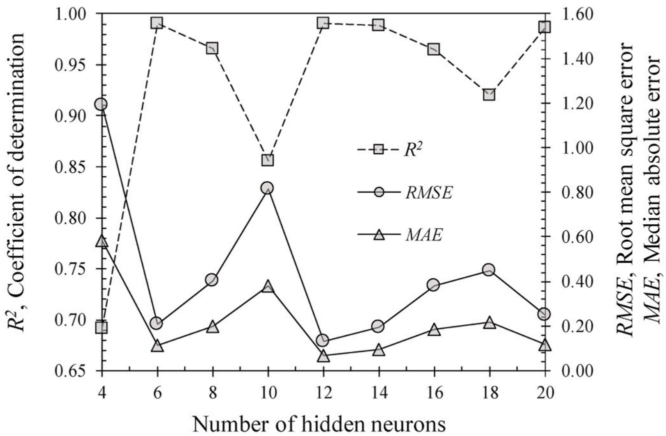

Fig. 20. The accuracy of ANN models according to the variation in the number of hidden neurons.

$$R^2 = 1 - \frac{SSR}{SST} \tag{9}$$

$$RMSE = \sqrt{\frac{1}{N}\sum_{i=1}^{N}(y_i - f(x_i))^2} \tag{10}$$

$$MAE = \frac{1}{N}\sum_{i=1}^{N}|y_i - f(x_i)| \tag{11}$$

where SSR is the regression sum of squares and SST is the total sum of squares. N is the number of data points in testing group, while y_i and $f(x_i)$ are the actual value and model's prediction, respectively.

6. Machine learning results

6.1. Results from ANN models

Fig. 20 shows the prediction accuracy from ANN models, which are trained from 4 to 20 neurons in their hidden layers. Especially, the performance is significantly enhanced when the number of nodes increases from 4 to 6. However, the model experiences a fluctuation in its accuracy with more than 6 nodes. A considerable fall is observed in the ANN performance, bottoming at 10 hidden nodes before being improved from 12 to 14 neurons. When the ANN model is trained with over 14 nodes, its accuracy again decreases, despite that there is an increasing tendency towards 20 hidden neurons. Having the highest value of R^2 as well as the lowest values of $RMSE$ and MAE, the ANN structure with 6 neurons in the hidden layer is considered optimal. Consequently, the equations for practical designs are proposed, as shown in Eqs. (12)–(17), utilizing the weight and bias values from the optimal ANN model, which are described explicitly in Table 6.

$$N_{c,LB} = -1.9669 \times N_1 + 1.467 \times N_2 - 3.5579 \times N_3 + 2.0172 \times N_4 - 1.8743 \times N_5 + 4.2619 \times N_6 + 1.8139 \tag{12}$$

$$N_{c,UB} = -1.8214 \times N_1 + 1.647 \times N_2 - 3.9722 \times N_3 + 2.0933 \times N_4 - 2.4403 \times N_5 + 4.3659 \times N_6 + 1.6452 \tag{13}$$

$$N_{s,LB} = 0.4056 \times N_1 + 0.1397 \times N_2 - 0.465 \times N_3 - 0.0095 \times N_4 - 0.4875 \times N_5 + 0.0748 \times N_6 + 0.3197 \tag{14}$$

Table 6
Weight and bias values from the optimal ANN model.

Node	W^1			b^1	W^2						b^2					
	ϕ	H/D	B/D		$N_{c,LB}$	$N_{c,UB}$	$N_{s,LB}$	$N_{s,UB}$	$N_{\gamma,LB}$	$N_{\gamma,UB}$						
1	−0.117	−0.355	0.128	0.628	−1.967	−1.821	0.406	0.419	−1.452	−1.572	1.814	1.645	0.320	0.275	0.807	0.775
2	0.780	0.329	−0.247	−1.713	1.467	1.647	0.140	0.130	2.895	2.679						
3	0.597	−0.071	−0.032	−1.740	−3.558	−3.972	−0.465	−0.474	−4.003	−3.799						
4	0.097	−0.018	−0.314	0.713	2.017	2.093	−0.010	−0.005	−0.720	−0.647						
5	−0.295	−0.507	0.019	0.445	−1.874	−2.440	−0.488	−0.547	−0.494	−0.342						
6	−0.087	0.006	0.051	0.802	4.262	4.366	0.075	0.061	0.835	0.860						

Table 7
Tuning ranges of six XGBoost hyper-parameters.

Hyper-parameters	Explanation	Tuning values	Default value
K	Maximum number of weak learners	50, 200, 400	None
ν	Learning rate	0.1, 0.3, 0.5, 0.7, 0.9	0.3
λ	Regularization factor	0.0, 0.5, 1.0, 5.0	1.0
r_s	Sub-sample ratio	0.25, 0.5, 0.75, 1.0	1.0
d_{max}	Maximum depth of each tree	5,6,7	6
γ	Minimum loss reduction for further division of nodes	0.0, 0.5, 2.0, 5.0	0.0

$$N_{s,UB} = 0.4193 \times N_1 + 0.1298 \times N_2 - 0.4738 \times N_3 - 0.0048 \times N_4 - 0.5471 \times N_5 + 0.0612 \times N_6 + 0.2751 \tag{15}$$

$$N_{\gamma,LB} = -1.4521 \times N_1 + 2.8948 \times N_2 - 4.0028 \times N_3 - 0.7203 \times N_4 - 0.4942 \times N_5 + 0.8353 \times N_6 + 0.8071 \tag{16}$$

$$N_{\gamma,UB} = -1.5722 \times N_1 + 2.6791 \times N_2 - 3.7994 \times N_3 - 0.6473 \times N_4 - 0.3415 \times N_5 + 0.8601 \times N_6 + 0.7754 \tag{17}$$

where:

$$N_1 = tansig\left(-0.117\phi - 0.3551\frac{H}{D} + 0.1278\frac{B}{D} + 0.6279\right)$$

$$N_2 = tansig\left(0.7804\phi + 0.3291\frac{H}{D} - 0.2471\frac{B}{D} - 1.7134\right)$$

$$N_3 = tansig\left(0.5968\phi - 0.0708\frac{H}{D} - 0.0317\frac{B}{D} - 1.7400\right)$$

$$N_4 = tansig\left(0.0972\phi - 0.0179\frac{H}{D} - 0.3137\frac{B}{D} + 0.7128\right)$$

$$N_5 = tansig\left(-0.2947\phi - 0.507\frac{H}{D} + 0.0193\frac{B}{D} + 0.4445\right)$$

$$N_6 = tansig\left(-0.0869\phi + 0.0063\frac{H}{D} + 0.0513\frac{B}{D} + 0.8017\right)$$

The following example illustrates the application of the optimized ANN model using the weight and bias values in Table 6 and Eqs. (12)–(17). The case under consideration has $\phi = 25^\circ$, $H/D = 2$, $B/D = 5$. The analysis from FELA provides the stability factors as follows: $N_{c,LB} = 2.107$, $N_{c,UB} = 2.120$, $N_{s,LB} = 0.015$, $N_{s,UB} = 0.009$, $N_{\gamma,LB} = 0.317$, and $N_{\gamma,UB} = 0.279$. The optimal ANN model, with six hidden nodes, is applied to compute stability factors as follows:

The outputs of the hidden layer are:

$$N_1 = tansig(-0.117 \times 25 - 0.3551 \times 2 + 0.1278 \times 5 + 0.6279) = -0.9826$$

$$N_2 = tansig(0.7804 \times 25 + 0.3291 \times 2 - 0.2471 \times 5 - 1.7134) = 1.0000$$

$$N_3 = tansig(0.5968 \times 25 - 0.0708 \times 2 - 0.0317 \times 5 - 1.7400) = 1.0000$$

$$N_4 = tansig(0.0972 \times 25 - 0.0179 \times 2 - 0.3137 \times 5 + 0.7128) = 0.9119$$

$$N_5 = tansig(-0.2947 \times 25 - 0.507 \times 2 + 0.0193 \times 5 + 0.4445) = -1.0000$$

$$N_6 = tansig\left(-0.0869\phi + 0.0063\frac{H}{D} + 0.0513\frac{B}{D} + 0.8017\right) = -0.8011$$

The outputs of the ANN model are:

$$N_{c,LB} = -1.9669 \times N_1 + 1.467 \times N_2 - 3.5579 \times N_3 + 2.0172 \times N_4 - 1.8743 \times N_5 + 4.2619 \times N_6 + 1.8139 = 1.9552$$

$$N_{c,UB} = -1.8214 \times N_1 + 1.647 \times N_2 - 3.9722 \times N_3 + 2.0933 \times N_4 - 2.4403 \times N_5 + 4.3659 \times N_6 + 1.6452 = 1.9613$$

$$N_{s,LB} = 0.4056 \times N_1 + 0.1397 \times N_2 - 0.465 \times N_3 - 0.0095 \times N_4 - 0.4875 \times N_5 + 0.0748 \times N_6 + 0.3197 = 0.0148$$

$$N_{s,UB} = 0.4193 \times N_1 + 0.1298 \times N_2 - 0.4738 \times N_3 - 0.0048 \times N_4 - 0.5471 \times N_5 + 0.0612 \times N_6 + 0.2751 = 0.0128$$

$$N_{\gamma,LB} = -1.4521 \times N_1 + 2.8948 \times N_2 - 4.0028 \times N_3 - 0.7203 \times N_4 - 0.4942 \times N_5 + 0.8353 \times N_6 + 0.8071 = 0.2942$$

$$N_{\gamma,UB} = -1.5722 \times N_1 + 2.6791 \times N_2 - 3.7994 \times N_3 - 0.6473 \times N_4 - 0.3415 \times N_5 + 0.8601 \times N_6 + 0.7754 = 0.2622$$

Compared to the results from FELA, the prediction formula proposed by the optimized ANN model is highly accurate and can be easily applied in practical calculations.

6.2. Results from XGBoost

In XGBoost, the architecture of each regression tree is decided during the training process, while other XGBoost hyper-parameters need to be determined before training models. These parameters can be categorized into two groups. The first one belongs to the algorithm-related, i.e.,

Table 8
Tuning results of six predictive models ($N_{c,LB}$, $N_{c,UB}$, $N_{s,LB}$, $N_{s,UB}$, $N_{\gamma,LB}$, $N_{\gamma,UB}$).

Predictive model	K_{max}	K	ν	λ	r_s	d_{max}	γ	R^2	RMSE	MAE
$N_{c,LB}$	400	101	0.1	0.5	0.25	6	0.0	0.9980	0.1386	0.0562
$N_{c,UB}$	400	124	0.1	0.5	0.25	7	0.0	0.9989	0.1114	0.0477
$N_{s,LB}$	200	134	0.1	2.0	0.25	7	0.0	0.9995	0.0071	0.0038
$N_{s,UB}$	400	315	0.1	2.0	0.25	7	0.0	0.9997	0.0058	0.0032
$N_{\gamma,LB}$	400	77	0.1	0.5	0.5	5	0.0	0.9974	0.1031	0.0457
$N_{\gamma,UB}$	400	120	0.1	2.0	0.5	5	0.0	0.9982	0.0834	0.0394

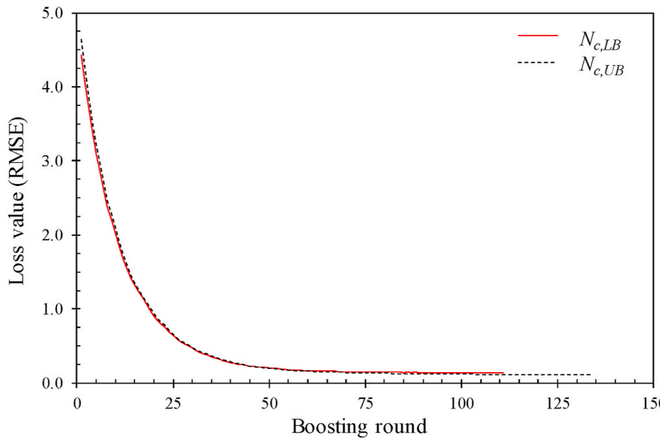

(a) $N_{c,\ LB}$ and $N_{c,\ UB}$ predictive models

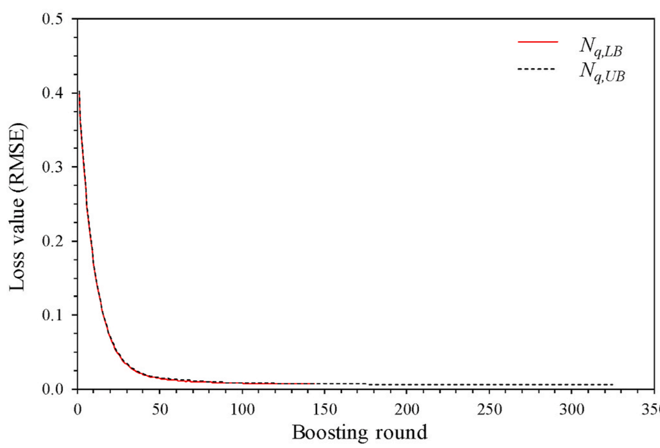

(b) $N_{s,\ LB}$ and $N_{s,\ UB}$ predictive models

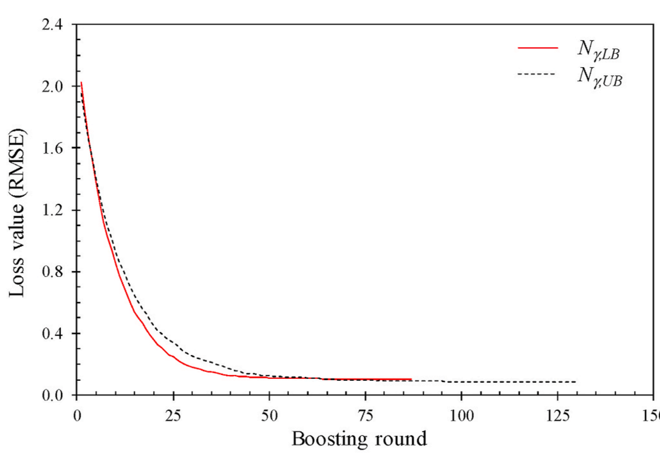

(c) $N_{\gamma\ LB}$ and $N_{\gamma\ UB}$ predictive models

Fig. 21. The decrease of *RMSE* during testing phase of six XGBoost models for predicting N_c, N_s, N_γ (LB and UB).

Table 9
Performance comparison between ANN and XGBoost models.

Model	R^2		*RMSE*		*MAE*	
	ANN	XGBoost	ANN	XGBoost	ANN	XGBoost
$N_{c,\ LB}$	0.9906	0.9980	0.3137	0.1386	0.2048	0.0562
$N_{c.\ UB}$	0.9907	0.9989	0.3323	0.1114	0.2106	0.0477
$N_{s,\ LB}$	0.9883	0.9995	0.0365	0.0071	0.0231	0.0038
$N_{s,\ UB}$	0.9872	0.9997	0.0379	0.0058	0.0224	0.0032
$N_{\gamma,\ LB}$	0.9945	0.9974	0.1508	0.1031	0.1010	0.0457
$N_{\gamma,\ UB}$	0.9923	0.9982	0.1713	0.0834	0.1149	0.0394

the number of trees (K), learning rate (ν), regularization factor (λ), and sub-sample ratio (r_s). The second one is the tree-related, i.e., the maximum depth of each tree (d_{max}) and the minimum loss reduction for further division (γ). Table 7 summarizes the tuning ranges of hyper-parameters applied in this study. Using a special technique called *Grid Search* from the package *scikit-learn* (Pedregosa et al., 2011; Lai et al., 2023), the optimal values of hyper-parameters in six predictive models are presented in Table 8.

With the tuned values of hyper-parameters, the performance of each XGBoost model is investigated during the training process by 5-fold cross-validation and early-stopping technique. The latter helps to reduce the risk of over-fitting, given the large number of weak learners. Specifically, the decrease of loss function *RMSE* in the testing phase is presented in Fig. 21. If the error of the testing stage is not improved after a preset value of the boosting round, the models will stop the boosting process. As a result, the number of regression trees can be reduced, as described in the second and third columns of Table 8. The high values of R^2, which are over 0.99 in six predictive models, proved the robust capacity of XGBoost in this regression problem.

6.3. The optimal method and sensitive analysis

To determine the optimal method, Table 9 compares the six predictive models ($N_{c,LB}$, $N_{c,UB}$, $N_{s,LB}$, $N_{s,UB}$, $N_{\gamma,LB}$, $N_{\gamma,UB}$) of the ANN models and XGBoost models. On average, the R^2 from the XGBoost is around 0.999, compared to about 0.99 from the ANN. In addition, XGBoost models have smaller values of *RMSE* and *MAE* than those in ANN models. Therefore, it can be concluded that the XGBoost technique outperforms the ANN technique in regression accuracy.

Despite the fact that the XGBoost method outperforms the ANN technique in regression accuracy, it cannot provide explicit predictive equations for practical designs. Besides, an ANN model can predict multi-targets, while the XGBoost needs tuning and training six models with different properties for six outputs (i.e., $N_{c,\ LB}$, $N_{c.\ UB}$, $N_{s,\ LB}$, $N_{s,\ UB}$, $N_{\gamma,\ LB}$, and $N_{\gamma,\ UB}$). Although the XGBoost models have better accuracy in prediction than the ANN models, the difference is just around 1 % ($R^2 =$ 0.999 for XGBoost compared to $R^2 = 0.99$ for ANN). Therefore, in this paper, the ANN is considered to be the optimal method.

Fig. 22 compares the prediction of the optimal ANN model with six hidden nodes using Eqs. (12)–(17) to the results obtained from FELA. The example provided in the previous section illustrated the application of these prediction formulas. Fig. 22 depicts the relationship between the six stability coefficients and the internal friction angle for various cases of B/D and H/D. It can be observed that the ANN model effectively captures the nonlinear relationship between the internal friction angle and the stability coefficients. Additionally, ANN prediction exhibits a high degree of consistency with the results from FELA.

Both ANN and XGBoost can address sensitive analysis, although their approaches are quite different. The former technique (ANN) is based on Garson's modified equation (Garson, 2013), as shown in Eq. (18). Here, I_j is the relative importance of the j_{th} input variable; N_i and N_h are the number of input and hidden neurons, respectively. Besides, W represents the connection weight; the superscripts i, h, and o denote input, hidden, and output layers, and the subscripts k, m, and n refer to input, hidden,

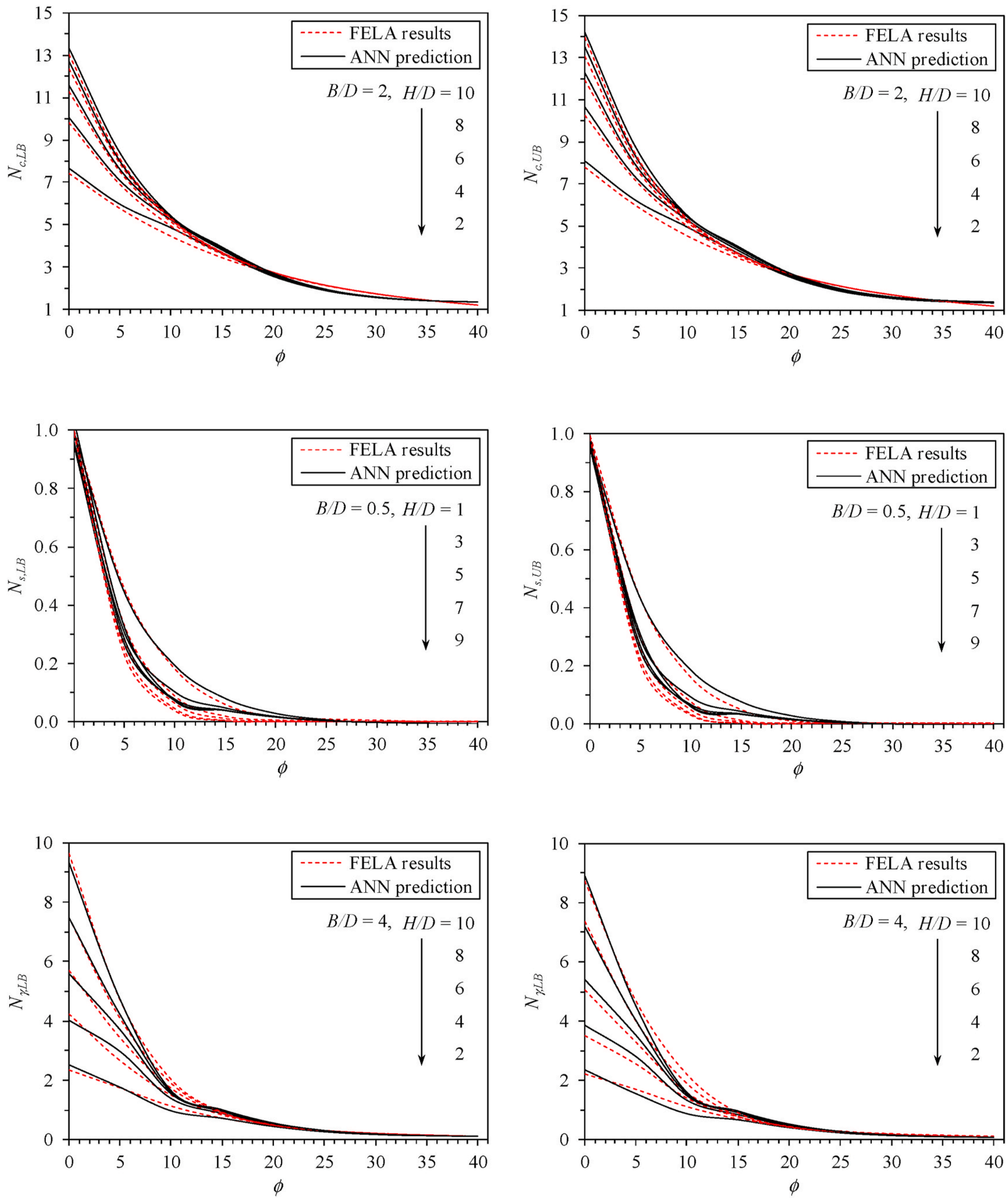

Fig. 22. Comparison between ANN prediction and FELA results.

and output neurons, respectively. Meanwhile, the latter technique (XGBoost) utilizes a term called *F-score*, representing the frequency of a feature that is used to divide non-leaf nodes of regression trees (Zhu et al., 2021; Lai et al., 2023).

$$I_j = \frac{\sum_{m=1}^{m=N_h}\left(\frac{\left|w^{ih}_{jm}\right|}{\sum\limits_{k=1}^{k=N_i}\left|w^{ih}_{km}\right|}\times\left|w^{ho}_{mn}\right|\right)}{\sum_{k=1}^{k=N_i}\left[\sum_{m=1}^{m=N_h}\left(\left|w^{ih}_{km}\right|\Big/\sum\limits_{k=1}^{k=N_i}\left|w^{ih}_{km}\right|\right)\times\left|w^{ho}_{mn}\right|\right]} \tag{18}$$

Fig. 23 presents the outcome of feature importance analysis for (ϕ, H/D, B/D). The relative importance index for both methods of ANN and XGBoost are shown in the figure. These results show similar trend in prediction between the ANN and XGBoost methods. Notably, ϕ is the one contributing most significantly in predicting six targets (i.e., $N_{c,\ LB}$, $N_{c.\ UB}$, $N_{s,\ LB}$, $N_{s,\ UB}$, $N_{\gamma,\ LB}$, and $N_{\gamma,\ UB}$). This is followed by H/D and B/D, respectively. It is also to be noted that each feature's importance remains quite stable with the multi-targets ANN model, whilst the index value fluctuates among different XGBoost models.

7. Conclusion

This paper has effectively studied the stability of 3D rectangular tunnels heading using a three-stability-factor approach, that is a subtle adaptation to Terzaghi's three bearing capacity factors. This method incorporates the principles of superposition and takes into consideration the influence of factors like cohesion, surcharge loads, and soil unit weight. Through the application of the Finite Element Limit Analysis (FELA) with upper and lower bounds, the research has yielded robust

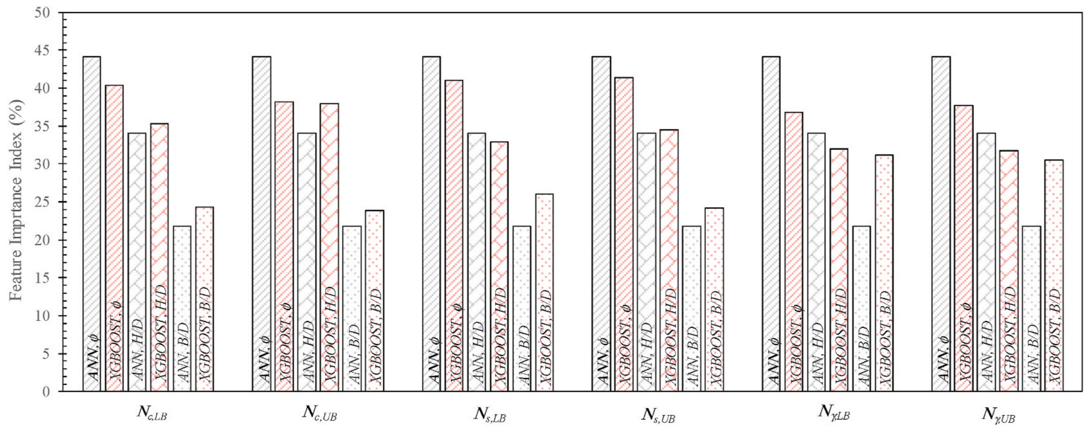

Fig. 23. Outcome of feature importance analysis (ANN and XGBoost) for (ϕ, H/D, B/D).

solutions for three crucial factors: the cohesion factor (N_c), surcharge factor (N_s), and unit weight factor (N_γ). These factors are dependent on the various parameters such as cover-depth ratio (H/D), width-depth ratio (B/D), and soil friction angle (ϕ). The comprehensive findings of (N_c, N_s, and N_γ) across various values of (ϕ, H/D, and B/D) have been presented in both graphical and tabular formats. With the principal of superposition, these results can be readily employed by professionals to estimate the minimum support pressure required within the inner tunnel. An example was illustrated to determine the appropriate support pressure required to maintain tunnel stability and design effective support systems to prevent tunnel face collapse during construction. Engineers can also assess the risk of tunnel collapse under specific soil conditions and surcharge loads, enabling them to develop tailored stability solutions for a given site. Additionally, it is useful for planning ground improvement techniques, such as the application of pre-excavation grouting or pressure control during tunnel boring.

Numerical comparisons of the three stability factors with published 3D circular tunnel heading results showed an excellent agreement. Building on this confidence, the study introduced Artificial Neural Networks (ANN) and XGBoost, to analyze the dataset generated by FELA results. Both ANN and XGBoost were able to accurately calculate feature importance scores, that revealed the contribution of each feature (input variable) to the model's predictions. This information is invaluable for engineers as it would help them to recognize which design parameters have the most influence on the tunnel stability, and base on this, to identify potential areas for further design improvement. In essence, the study demonstrates the effectiveness of machine learning in providing insights for better tunnel design.

CRediT authorship contribution statement

Suraparb Keawsawasvong: Supervision, Software, Formal analysis, Data curation, Conceptualization. **Jim Shiau:** Writing – review & editing, Validation, Investigation, Conceptualization. **Nhat Tan Duong:** Writing – original draft, Validation, Software, Investigation, Formal analysis, Data curation. **Thanachon Promwichai:** Writing – original draft, Validation, Formal analysis, Data curation. **Rungkhun Banyong:** Writing – original draft, Visualization, Formal analysis, Data curation. **Van Qui Lai:** Writing – review & editing, Writing – original draft, Validation, Methodology, Data curation, Conceptualization.

Declaration of competing interest

The authors declare that they have no known competing financial interests or personal relationships that could have appeared to influence the work reported in this paper.

Acknowledgment

We acknowledge Ho Chi Minh City University of Technology (HCMUT), VNU-HCM for supporting this study.

References

Abbo, A.J., Wilson, D.W., Sloan, S.W., Lyamin, A.V., 2013. Undrained stability of wide rectangular tunnels. Comput. Geotech. 53, 46–59.
Anagnostou, G., Kovári, K., 1996. Face stability conditions with earth-pressure-balanced shields. Tunn. Undergr. Space Technol. 11 (2), 165–173.
Atkinson, J.H., Mair, R.J., 1981. Soil mechanics aspects of soft ground tunnelling. Ground Eng. 14 (5).
Azim, R.A., 2022. A new correlation for calculating wellhead oil flow rate using artificial neural network. Artif. Intel. Geosci. 3, 1–7.
Bhattacharya, P., Dutta, P., 2023. Stability of rectangular tunnel in anisotropic cohesionless soil under steady-state groundwater flow. European J. Environ. Civil Eng. 27 (4), 1596–1616.
Chen, T., Guestrin, C., 2016. Xgboost: a scalable tree boosting system. In: Proceedings of the 22nd Acm Sigkdd International Conference on Knowledge Discovery and Data Mining, pp. 785–794.
Chen, W.F., Liu, X.L., 2012. Limit Analysis in Soil Mechanics. Elsevier.
Drucker, D.C., Prager, W., Greenberg, H.J., 1952. Extended limit design theorems for continuous media. Q. Appl. Math. 9 (4), 381–389.
Garson, G.D., 2013. Path Analysis. Asheboro, NC. Statistical Associates Publishing.
Huynh, Q.T., Lai, V.Q., Shiau, J., Keawsawasvong, S., Mase, L.Z., Tra, H.T., 2022. On the use of both diaphragm and secant pile walls for a basement upgrade project in Vietnam. Innovat. Infrastruct. Sol. 7 (17), 2022.
Keawsawasvong, S., Ukritchon, B., 2022. Design equation for stability of a circular tunnel in anisotropic and heterogeneous clay. Undergr. Space 7 (1), 76–93.
Kingma, D.P., Ba, J., 2014. Adam: a method for stochastic optimization. arXiv: 1412.6980v9.
Krabbenhoft, K., Lyamin, A.V., Sloan, S.W., 2007. Formulation and solution of some plasticity problems as conic programs. Int. J. Solid Struct. 44 (5), 1533–1549.
Lai, V.Q., Nguyen, T.K., Shiau, J., Keawsawasvong, S., Bui, T.S., Tran, M.N., 2023. Coupling FEA with XGBoost model for estimating uplift resistance of circular anchor in NGI-ADP soils. Geotech. Geol. Eng. 1–15.
Lai, V.Q., Shiau, J., Van, C.N., Tran, H.D., Keawsawasvong, S., 2022. Bearing Capacity of Conical Footing on Anisotropic and Heterogeneous Clays Using FEA and ANN. Marine Georesources & Geotechnology, pp. 1–18.
Lai, V.Q., Lai, F., Yang, D., Shiau, J., Yodsomjai, W., Keawsawasvong, S., 2022. Determining seismic bearing capacity of footings embedded in cohesive soil slopes using multivariate adaptive regression splines. Int. J. Geos. Ground Eng. 8 (4), 46.
Liang, J., Liu, W., Yin, X., Li, W., Yang, Z., Yang, J., 2024. Experimental study on the performance of shield tunnel tail grout in ground. Undergr. Space 20, 277–292. https://doi.org/10.1016/j.undsp.2024.07.001.
Liu, W., Zhang, X., Wu, B., Huang, Y., 2024. An improved mechanism for partial blowout instability of tunnel face in large slurry shield-driven tunnels. Acta Geotechnica 19 (5), 3021–3038. https://doi.org/10.1007/s11440-024-02229-8.
Lyamin, A.V., Sloan, S.W., 2002a. Lower bound limit analysis using non-linear programming. Int. J. Numer. Methods Eng. 55 (5), 573–611.
Lyamin, A.V., Sloan, S.W., 2002b. Upper bound limit analysis using linear finite elements and non-linear programming. Int. J. Numer. Anal. Methods GeoMech. 26 (2), 181–216.
Nguyen, D.K., Nguyen, T.P., Ngamkhanong, C., Keawsawasvong, S., Lai, V.Q., 2023a. Bearing capacity of ring footings in anisotropic clays: FELA and ANN. Neural Comput. Appl. 1–22.
Nguyen, D.K., Nguyen, T.P., Ngamkhanong, C., Keawsawasvong, S., Nguyen, T.K., 2023b. Prediction of uplift resistance of circular anchors in anisotropic clays using MLR, ANN, and MARS. Appl. Ocean Res. 136, 103584.

Pandey, V.H.R., Kainthola, A., Sharma, V., Srivastav, A., Jayal, T., Singh, T.N., 2022. Deep learning models for large-scale slope instability examination in Western Uttarakhand, India. Environ. Earth Sci. 81 (20), 487.
Pedregosa, F., Varoquaux, G., Gramfort, A., Michel, V., Thirion, B., Grisel, O., et al., 2011. Scikit-learn: machine learning in Python. J. Mach. Learn. Res. 12, 2825–2830.
Qarmout, M., König, D., Gussmann, P., Thewes, M., Schanz, T., 2019. Tunnel face stability analysis using Kinematical Element Method. Tunn. Undergr. Space Technol. 85, 354–367.
Rozante, J.R., Ramirez, E., Ramirez, D., Rozante, G., 2023. Improved frost forecast using machine learning methods. Artif. Intell. Geosci. 4, 164–181.
Sangjinda, K., Banyong, R., Alzabeebee, S., Keawsawasvong, S., 2023. Developing soft-computing regression model for predicting bearing capacity of eccentrically loaded footings on anisotropic clay. Artif. Intel. Geosci. 4, 68–75.
Shahin, M.A., Jaksa, M.B., Maier, H.R., 2001. Artificial neural network applications in geotechnical engineering. Aust. Geomech. 36 (1), 49–62.
Shekar, P.R., Mathew, A., Yeswanth, P.V., Deivalakshmi, S., 2024. A combined deep CNN-RNN network for rainfall-runoff modelling in Bardha Watershed, India. Artif. Intel. Geosci., 100073
Shiau, J., Mahalingasivam, K., Chudal, B., Keawsawasvong, S., 2022. Pipeline burst–related soil stability in collapse condition. J. Pipeline Syst. Eng. Pract. 13 (3), 04022019.
Shiau, J., Al-Asadi, F., 2022. Stability factors fc, fs, and Fγ for twin tunnels in three dimensions. Int. J. GeoMech. 22 (3), 04021290.
Shiau, J., Al-Asadi, F., 2020a. Two-dimensional tunnel heading stability factors Fc, Fs and Fγ. Tunn. Undergr. Space Technol. 97, 103293.
Shiau, J., Al-Asadi, F., 2020b. Determination of critical tunnel heading pressures using stability factors. Comput. Geotech. 119, 103345.
Shiau, J., Al-Asadi, F., 2020c. Twin tunnels stability factors F c, F s and F γ. Geotech. Geol. Eng. 39, 335–345.
Shiau, J., Al-Asadi, F., 2020d. Stability analysis of twin circular tunnels using shear strength reduction method. Géotech. Lett. 10 (2), 311–319.
Shiau, J., Keawsawasvong, S., 2022. Producing undrained stability factors for various tunnel shapes. Int. J. GeoMech. 22 (8), 06022017.
Shiau, J., Yu, H.S., 2000. Shakedown analysis of flexible pavements. Proc. of the John Booker Memorial Symposium (ed DW Smith & JP Carter) 26, 643–653.
Sloan, S.W., 1988. Lower bound limit analysis using finite elements and linear programming. Int. J. Numer. Anal. Methods GeoMech. 12 (1), 61–77.
Sloan, S.W., 1989. Upper bound limit analysis using finite elements and linear programming. Int. J. Numer. Anal. Methods GeoMech. 13 (3), 263–282.
Sloan, S.W., 2013. Geotechnical stability analysis. Geotechnique 63 (7), 531–571.
Sloan, S.W., Assadi, A., 1991. Undrained stability of a square tunnel in a soil whose strength increases linearly with depth. Comput. Geotech. 12 (4), 321–346.
Vermeer, P.A., Ruse, N., Marcher, T., 2002. Tunnel heading stability in drained ground. Felsbau 20 (6), 8–18.
Wilson, D.W., Abbo, A.J., Sloan, S.W., 2015. Undrained stability of tall tunnels. In: Oka, F., Murakami, A., Uzuoka, R., Kimoto, S. (Eds.), Computer Methods and Recent Advances in Geomechanics, pp. 447–452.
Wilson, D.W., Abbo, A.J., Sloan, S.W., Lyamin, A.V., 2011. Undrained stability of a circular tunnel where the shear strength increases linearly with depth. Can. Geotech. J. 48 (9), 1328–1342.
Wu, B., Liu, W., Chian, S.C., Yan, J., Cheng, C., 2024. Analysis of working face stability of longitudinally inclined shield driven tunnels in frictional soils. Tunn. Undergr. Space Technol. 144, 105579. https://doi.org/10.1016/j.tust.2023.105579.
Xiao, Y., Zhao, M., Zhang, R., Zhao, H., Peng, W., 2019a. Stability of two circular tunnels at different depths in cohesive-frictional soils subjected to surcharge loading. Comput. Geotech. 112, 23–34.
Xiao, Y., Zhao, M., Zhang, R., Zhao, H., Wu, G., 2019b. Stability of dual square tunnels in rock masses subjected to surcharge loading. Tunn. Undergr. Space Technol. 92, 103037.
Yamamoto, K., Lyamin, A.V., Wilson, D.W., Sloan, S.W., Abbo, A.J., 2011a. Stability of a circular tunnel in cohesive-frictional soil subjected to surcharge loading. Comput. Geotech. 38 (4), 504–514.
Yamamoto, K., Lyamin, A.V., Wilson, D.W., Sloan, S.W., Abbo, A.J., 2011b. Stability of a single tunnel in cohesive–frictional soil subjected to surcharge loading. Can. Geotech. J. 48 (12), 1841–1854.
Zhang, R., Xiao, Y., Zhao, M., Zhao, H., 2019. Stability of dual circular tunnels in a rock mass subjected to surcharge loading. Comput. Geotech. 108, 257–268.
Zhu, X., Chu, J., Wang, K., Wu, S., Yan, W., Chiam, K., 2021. Prediction of rockhead using a hybrid N-XGBoost machine learning framework. J. Rock Mech. Geotech. Eng. 13 (6), 1231–1245.